PCCP

Accepted Manuscript




ROYAL SOCIETY OF CHEMISTRY

www.rsc.org/pccp

Journal Name

ARTICLE

# Synthesis of Ceria Based Superhydrophobic Coating on Ni20Cr Substrate via Cathodic Electrodeposition

F. Pedraza, S.A . Mahadik*, and B. Bouchaud,

Received 00th January 20xx,
Accepted 00th January 20xx

DOI: 10.1039/x0xx00000x

www.rsc.org/

In this work, superhydrophobic cerium oxide coating surface (111) with dual scale texture on Ni20Cr substrate is obtained by combination of electropolishing the substrate and subsequent cathodic electrodeposition and long-term vacuum relaxation. The formation of hierarchical $CeO_2$ structures is controllable by varying the substrate roughness, and electropolishing period. The results indicated that at the optimal condition, the surface of the cerium oxide coating showed a superhydrophobicity with a great water contact angle (151.0±1.4°) with Gecko state. An interface model for electropolishing of substrate surface in cerium nitrate medium is proposed. We expect that this facile process can be readily and widely adopted for the design of superhydrophobic coating on engineering materials.

## 1. Introduction

Artificial superhydrophobic surfaces that mimic those of natural materials, such as the lotus (nelumbo nucifera) leaf, which is extremely difficult to wet, have drawn extensive interest for self-cleaning surfaces, ice-repellent coatings, antifouling surface reduced oxidation, anticorrosion and improved efficiency of marine vehicles[1-4]. In the case of the lotus leaf, the superhydrophobicity can be attributed to both the nano/micro scale rough morphology and thin layer of nonpolar epicuticular wax material [5]. Likewise, artificially prepared superhydrophobic surfaces can be successfully improved through controlled roughness or surface modification processes that lower the surface free energy. In this view, various methods involving the use of sol-gel coating using surface modification [6], fibrous surfaces [7], plasma treatment [8], template method [9], and rough block copolymer surfaces [10], have been focused to fabricate artificial superhydrophobic surfaces.

Some studies have been focused on the preparation of superhydrophobic $CeO_2$ surfaces by means of electrodeposition and surface modification methods owing to its hierarchical structures etc. For instance, Ishizaki's group fabricated a durable and chemically stable superhydrophobic $CeO_2$ film with dandelion like structure grown on Mg alloy via combination of surface modification with fluroalkylsilane and immersion method [11]. Duan et.al.[12] reported on the synthesis of superhydrophobic cotton fabricated from cerium oxide particles and further modified with dodecafluroheptyl-propyl trimethoxysilane (DFTMS) and demonstrated their UV protection for textiles. However, the low-surface free energy film material formed on rough metal surfaces with the surface modification method has limited thermally stability and poisonous nature of organic groups, which can restrict future industrial and domestic applications. Martinez et al. reported that a hydrophobic surface was obtained on electrodeposited $CeO_2$ on zinc after X-ray photoelectron spectroscopy analysis (XPS)[13]. However, it remained unclear whether this phenomenon arose from the vacuum itself or from the ionic bombardment carried out in the XPS chamber. More recently, Varanasi et al. successfully produced a hydrophobic rare earth metal oxide (REOs) material for high temperature applications [14]. However, these procedures also used a surface modification method. Although the without chemical modification method used to create low energy surface

*Address here . Université de La Rochelle, Laboratoire des Sciences de L'Ingénieur pour l'Environnement (LaSIE, UMR-7356 CNRS-Université de La Rochelle), Avenue Michel Crépeau, 17042 La Rochelle cedex 01, France.*
fernando.pedraza@univ-lr.fr,
Superhydrophobicmaterial2100@gmail.com,
baptiste.bouchaud01@univ-lr.fr

† Footnotes relating to the title and/or authors should appear here.
Electronic Supplementary Information (ESI) available: [details of any supplementary information available should be included here]. See DOI: 10.1039/x0xx00000x

not sufficient for preparation superhydrophobic surface, the enhancement required to prepare the inorganic superhydrophobic coating was too complex. Therefore, the simple synthesis of superhydrophobic coating method with inorganic $CeO_2$ material that would be very advantageous for high temperature application is challenged.

In view of this, we design in this paper a simple method for fabricating superhydrophobic $CeO_2$ (111) surface on Ni20Cr superalloy. The fabrication process of superhydrophobic surface mainly contains three steps: mechanical and electropolishing, cathodic electrodeposition of $CeO_2$ followed by dehydration and further long-term relaxation in ultra-high vacuum.

## 2. Experimental Section

### 2.1. Materials and Reagents

Cerium (III) nitrate hexahydrate (Mw≈434.22, 99.9 %) was obtained from Fluka chemical. Ethylene glycol (99.5%) was purchased from Fluka and Glycerin (99%), diodomethane (99%), formamide (99.5%) and potassium chloride (99.9%) were purchased from Sigma Aldrich. Ni20Cr material was purchased from Goodfellow in the rod form with 99.98% of purity (Al=1000 ppm, Fe=2000 ppm, Mg=2000 ppm, Si=1.5 wt %, Cr=18-20 wt%, Ni balance). Pure water with a resistivity higher than 18.2 MΩcm was used in all experiments, and was obtained by a three-stage Millipore Milli-Q PlusV25 purification system.

### 2.2. Surface Treatment on Ni20Cr superalloy Substrates

The Ni20Cr superalloy substrates in the disc form (diameter of 12.7 mm) were mechanically polished using different grades of SiC papers grit, then ultrasonicated in acetone and finally in ethanol for 20 min, respectively. After ultrasonication, the substrates were dried with hot air and observed under the light microscope. The surfaces appeared free of embedded SiC particles.

In order to study the influence of the surface roughness and composition on the wettability, different surfaces were prepared by mechanical finish with different grades papers (SiC#180, 320, 600, 800, 1200 and 2400) and different electropolishing periods (0, 1, 2 and 5 min). Electropolishing process was carried out in the same electrolytic solution employed for coating deposition (0.1 M of Ce(NO3)3, 6H2O in water – pH≈5) at room temperature and by applying an anodic current of J=0.2 $mAcm^{-2}$.

### 2.3. Synthesis of Cerium Oxide Coatings

A simple three-electrode cell was used for electrodeposition in these experiments. The reference electrode of saturated calomel electrode (SCE) was put in contact with electrolytic solution though a Luggin extension. The counter-electrode was a large (L×H=14×5 $cm^2$) Pt grid (99.99%) and the cathode a small (A= 2.3 $cm^2$) Ni20Cr surface. The electrochemical experiments were carried out in the galvanostatic mode at room temperature without stirring, thus avoiding convection phenomena [15]. A cathodic current density of J= -0.5$mAcm^{-2}$ was applied for 10 min at room temperature. After electrodeposition, the coating was brought out of salt solution, washed carefully with ethanol and dried in air.

### 2.4. Characterization

The hierarchical surface morphologies of coatings on substrate of Ni20Cr superalloy were recorded by Field Emission scanning electron microscopy (FE-SEM) with Energy Dispersive X-ray spectroscopy (EDS) on a Quanta-200F operated at 20 kV and partial vacuum (0.9 to 1.3 mbar). The oxygen vacancies of the coatings were measured based on spatial correlation model applied to the $F_{2g}$ Ce-O vibration Raman band of $CeO_2$ located at 450 $cm^{-1}$[16]. The Raman analysis were performed with a high resolution Raman spectroscopy (Horiba JobinYvon) with He-Ne laser (632.82 nm). The XRD patterns of the samples were recorded with a Bruker D8 Advance ($CuK_\alpha$), in θ-2θ mode and at grazing incidence 5°. The crystal size of the coated $CeO_2$ material was calculated by using Debye–Scherrer equation applied to the diffraction peak associated with the $CeO_2$(111) plane [17]. The mean surface roughness (Ra) was measured with a Mitutoyo Surftest SJ-201 M (Japan) portable roughness tester instrument. The surface roughness is an average taken from 10 measurements. The water contact angles (WCAs) of surfaces were measured at ambient temperature on a contact meter (Advex Instruments, Czech Republic) with accuracy ±0.5°. The sessile drop method was adopted for static contact angles measurements by putting down 0.5 µL drops with a high performance micro volume pipette (Vitrum). For the contact angle measurements, the electropolished substrates were used after 10 minutes of ultrasonication treatment in ethanol. In the case of electrodeposited (superhydrophilic) coatings, the measurements



 

were performed after 7 days of dehydration in a dessicator at room temperature. The measurements of surface free energy were carried out based on acid-base regression model using five different liquids including deionised water, glycerin, diiodomethane, ethylene glycol and formamide.

## 3. Results and Discussion

### 3.1. Effect of Electropolishing on the Surface Properties of Ni20Cr Substrates

P. Wang found that optimal smooth surfaces were important for obtaining optimum and well ordered surface features during the electrodeposition processing [18]. Therefore, electropolishing of the ground (SiC#320) Ni20Cr alloy was studied as a first attempt to enhance its surface quality and reduce its roughness. Figure 1(a-d) gathers the SEM and EDS results of Ni20Cr alloy after mechanical polishing and with increasing electropolishing periods. After mechanical polishing, the surface display considerable streaks that tend to disappear with electropolishing period to result in a more even and featureless surface. The EDS analysis also highlight that electropolishing also results in the dissolution of Fe, Cr and Si from Ni20Cr substrates. The surface initiates metal ions dissolution at 1 min electropolishing process and disappear metal ions from surface after 5 min. It is also supported by mass losses are depicted in figure 6. Therefore, the levelling and dissolution action drastically change the values of water contact angles at the surface of Ni20Cr. Indeed, the contact angles (θ) increase progressively from 36.9±0.7° for the mechanically polished to 53.4±1.6°, 42.5±1.2°, and 37.0±1.1° after electropolishing for 1, 2 and 5 min, respectively. From above study, it is confirmed that the electropolishing process produces significant influence on the physics and chemical properties of surface Ni20Cr substrates.

### 3.2. Effect of Electropolishing on Growth of $CeO_2$ Coating Texture and Their Surface Properties

The mechanisms of cathodic electrogeneration including step of electrogeneration fallowed by ceria-based coatings depositeing from aqueous solutions of cerium nitrates are well established.[19-22] These are based on the alkalinization of the interface with hydroxyls and subsequent precipitation of the cerium hydroxides (reactions <1> and <2>):

$$Ce^{3+} + 3HO^- \rightleftharpoons Ce(OH)_3 \quad (1)$$

$$4Ce^{3+} + O_{2(g)} + 4HO^- + 2H_2O \rightleftharpoons 4Ce(OH)_2^{2+} \quad (2)$$

The hydroxides then partially dehydrate and/or oxidize at the coating surface according to Equation <3> and<4>:

$$Ce(OH)_3 \rightarrow CeO_2 + H_3O^+ + e^- \quad (3)$$

$$Ce(OH)_2^{2+} + 2HO^- \rightarrow CeO_2 + 2H_2O \quad (4)$$

According to the surface studies carried out by Martinez et al. [13], the outermost surface of the coating is mostly composed of $Ce(OH)_3$ with some contribution from $Ce(OH)_4$ after oxidation of $Ce(OH)_3$whereas the internal layers may be mostly composed of $CeO_2$ following dehydration.

The insets of Figure 2(a-d) depict the photographs of the ceria coatings grown on the surfaces of Ni20Cr substrate electropolished for different periods (0-5 min). The colour evolves from gloomy blue to slightly sharp blue with the increase of electropolishing period. Also, regardless of the electropolishing period, the coatings appear to be free of cracks that often appear by hydrogen bubbling [20], fast growth kinetics [23] and by shrinkage upon dehydration.[24] This is likely due to a lower level of interfacial stress resulting from the concentration gradient of dissolved metal ions over the smoothened streaks[25]. These statements are better observed at higher magnifications in the SEM (Figure 2(a-d)). The surface of mechanically polished is well covered with a dense network of needle-like textures and is partly cracked. In contrast, cracking of the coatings disappears and the surface appears less covered with increasing electropolishing period. This evidence also confirmed from EDS analysis are depicted in Figure 3, where the contribution of the substrate elements is greater than that of the coating elements. We found that as deposited ceria coatings have an over-stoichiometric Ce/O ratio on the surface, increasing up to 0.155. They accredited this irregularity to excess oxygen occurs on the surface arising from the electrodeposition. Therefore, Ce/O ratio drops progressively with increasing electropolishing period can positively influence wettability, as it provides minimum sites for hydrogen bonding with water drop and generate hydrophobic nature [26].

According to the Raman spectra depicted in Figure 4(a), the electrodeposits consist of the oxygen-defective ceria-based layers that crystallized as $CeO_2$ with a pure cubic fluorite phase (111) reflection displayed in the XRD pattern from Figure 4(b). From above analysis, crystallite size and number of oxygen vacancies

were recorded in Table 1. Irrespective of the method, it appears that the crystallite size increases with increasing electropolishing period. Therefore, the density of oxygen vacancies in turn decreases from $2.13\times10^{22}$ $cm^{-3}$ to $1.47\times10^{22}$ $cm^{-3}$. Water dissociation has been reported to be much less favourable on stoichiometric $CeO_2$ (111) as compared to non-stoichiometric surfaces below room temperature. Indeed, the surface oxygen vacancies can act as active sites for water dissociation and hydrophilic $^{-}OH$ adsorption on the nano crystalline ceria coating surface [27]. Therefore; the greater the density of oxygen vacancies, the lower the contact angle should be. This is clearly confirmed through the values of contact angle of coating after mechanically polishing with SiC#320 paper grit. It display a lower contact angle 30.0±0.6° as compared to the electropolished coated surfaces (51.0±1.5° for 1 min, 68.0±2.0° for 2 min, and 98.0±4° for 5 min) in agreement with the reduction of oxygen vacancies predicted from table 1. Thus, the combination of decreased roughness and more stoichiometric $CeO_2$ results in greater hydrophobicity on partially dehydrated coating surfaces. Such coating surfaces need deposited on optimal roughness and undertake long-term relaxation to reach highly reduced surface before inherent superhydrophobicity can be strictly established.

## 3.4. Development of Superhydrophobic Surface

### 3.4.1. Surface Interface Model and Optimal Surface Conditions for Superhydrophobicity on Ni20Cr Superalloy Surface

Wettability is a function of roughness is known as a universal phenomenon. Early in 1936 Wenzel [28] and 1944 Cassie–Baxter [29] showed the contact angles increased with surface roughness. Although extensive and extended studies on the relation roughness between wettability on solid surfaces have been carried out, the earlier work just focused on theoretical relations and their trend in experimental observations. So far, there are few investigations about the substrate roughness required to build up hierarchically structured superhydrophobic surfaces. [30] In order to show the essential relationship of wettability and roughness, we propose a simple idealized surface interface model for the substrate roughness with help of mechanical polishing and electropolishing process. Therefore, we turned our attention to the optimization of surface roughness on Ni20Cr substrate. By applying this surface interface model depicted in Figure 5(a-b) to obtain optimal surface conditions for superhydrophobic surface build on Ni20Cr superalloy, better wettability results could be obtained. Moreover, we applied the surface interface model to choose the appropriate combination of mechanical polishing and electropolishing conditions.

Figure 5(a) shows wettability is a function of surface roughness, which is obtained by appropriate combination of mechanical polishing, and electropolishing conditions. The contact angles values raise with roughness up to certain limit ($\phi_c$=0.1114 μm) and decreases beyond it. In particular, initially contact angles increased for substrate surface obtained by using polishing paper grit ranging from 180 to 800. It is due to capillarity force normal to concave menisci between grooves and cavities. Then, the contact angle decreased for paper grit ranging from 800 to 2400 due to capillarity forces formed along convex menisci. The droplet spreaded until its radius reached equilibrium conditions by a combined effect of capillary, gravitational, and viscous forces.

In the case of electropolishing (1 to 5 min) plus mechanical polishing (Fig. 6b), a similar trend of a contact angle with polishing grade paper is observed. This implies that the contact angle is governed by mechanical polishing. However, the values of contact angle change compared to the as-mechanically polished surfaces. In the case of 1 min electropolishing period, the highly rough surface appears appropriately smoothened, which is favourable for higher wettability and cause to gain higher contact angles [31]. However, further increase of the electropolishing periods to 2 min and 5 min, lowers the contact angle by dissolution of the coating (Figure 6) as it was confirmed in the previous SEM images of Figure 1, where effective etching at top part rather than at valley part of the coating textures results in a smoothened appearance of the coated surface. According to the Wenzel's model, the water droplet forms a curved surface linking the boundary of the liquid and air for the capillary force action [32]. Therefore, the water droplet can hardly wet the rough substrate surface for the obstructive effect of mechanical polished line and electropolishing process generate the best surface wettability ability. This surface interface model play an important role in designing superhydrophobic cerium oxide coating on Ni20Cr substrate, reduces optimisation periods, and understands that significant values can be used each condition. This model can be useful in designing superhydrophobic coating on appropriate micro scale rough surface of wide variety engineering materials. In this particular case, it appears that the Ni20Cr substrate show maximum

contact angles for a combination of mechanically polishing with SiC#800 paper grit and electropolishing for 1 min.

**3.4.2. Interaction of Coating Surfaces under Vacuum**

During dehydration, the bonding configuration of surface cerium oxy-hydroxydes after electrodeposition [15,21,23] may promote a particular decomposition pathway under oxygen-lean conditions[33]. The transition is made possible by continuous loss of surface oxygen atoms by dehydration and or oxidation represented by Equations <3> and <4>. Here, the , long-term vacuum relaxation at $9.7\times10^{-7}$ mbar for 60 hours of the electrodeposited cerium oxide generated an transitional $Ce(OH)_4$ phase that rearranged in to well-ordered stoichiometric and most stable $CeO_2$(111) surface[13]. The surface transition from the O-terminated (111) to the most stable and highly reduced Ce-terminated $CeO_2$(111)surface is more slowly with the presence of many intermediate defective surface structures only found at vacuum relaxation and less than room temperature[34-36]. Figure 9(a-b) shows the FE-SEM images before and after vacuum relaxation of $CeO_2$ coating on optimal condition (mechanically polished by 800 paper grit + 1 min of electropolishing). It is quite difficult find out changes in the morphology of the coatings and the EDS surface analysis displayed minor differences (≈ 4%) in the Ce/O ratios, which were assumed to account for dehydration of coating as also proposed Borowiak et al. [37]. The surface oxygen can negatively influence on their wettability. It is clear that surface relaxation in an oxygen lean, ultra-high vacuum (UHV) relaxation causes increases in Ce/O ratio in ceria owing to reduces in oxygen amount and changed surface chemistry, which is consistent with results of Zhang et al[38]. Finally, it caused to a decrease in the surface Ce/O ratio in ceria is accompanied by a consequent boost in water contact angle (WCA).

In spite of this minor EDS chemical, the Raman spectra and the XRD clearly indicate that the crystal size and oxygen vacancies evolved with vacuum relaxation (Table 2) the crystal sizes increased while the oxygen vacancies decreased. In particular, comparative Raman spectra before and after vacuum (Figure 8(a)) display significant differences. The peak at 456 $cm^{-1}$ associated with $CeO_2$(111) becomes more symmetrical and therefore of the amount of oxygen vacancies drop from $1.88\times10^{22}$ to $1.54\times10^{22}$ $cm^{-3}$ due to the conversion into more stable stoichiometric $CeO_2$ (111) surface. In addition, the trapped nitrate anions desorbed while the hydroxyl groups in the range of 3000-3600 $cm^{-1}$ were hardly observed after vacuum, which confirms that the coating dehydrated and stabilized a Ce-terminated $CeO_2$(111) surface so that water molecule adsorption is reduced significantly. Therefore, we successfully demonstrate the crucial importance of vacuum relaxation in discovering the superhydrophobicity of ceria.

**3.4.3. Contact Angle and Surface Free Energy Measurement of Superhydrophobic Coating Surface**

Generally, metallic and ceramic surfaces are hydrophilic nature due to co-ordination number and excess of surface defects. It will attempt to accomplish of octets by water molecule dissociation at the interfacial plane [39]. In our study, the vacuum dehydration of $CeO_2$ coatings surface highly reduces in to low free energy surface with minimum surface defects, and effectively enhanced hydrophobicity. A water droplet with a size much larger than the aforementioned microstructures partially penetrates into the grooves among the hierarchical textures, but is quite suspended on the rough structures with superhydrophobicity without any sliding angle, it is also known as Gecko state. It form heterogeneous surfaces combined of solid textures and air. This condition is called a Cassie Baxter state. Cassie-Baxter Equation [29] on a rough texture of composite material surfaces partially wet by liquids droplets is given by Equation <5>

$$COS\theta_{CB} = f_s \cos\theta - (f_a) \quad (5)$$

Where $\theta_{CB}$ and θ represent the contact angles on the stoichiometric $CeO_2$ (111) rough and smooth surfaces respectively, and $f_s$ and $f_a$ are the area fractions of the solid and air on the surface respectively. We know relation $f_s+f_a=1$ and observed value of experimental contact angle is $\theta_c=151^o$, the theoretical value of $\theta=58.25^o$ was calculated using experimental value of $\theta_{CB.}$ The value of $f_s$ and $f_a$ are estimated at 0.082 and 0.918, respectively. These data indicate that, when a water droplet is placed on the superhydrophobic $CeO_2$ surface, approximately 8.2% serves as the contact area between the water droplet and the solid surface, and the remaining 91.8 % serves as the contact area between the water drop with air.

The surface free energy of the superhydrophobic cerium oxide can be calculated according to so called acid–base method (equation (6))[40]:

$$\frac{(1+\cos\theta_i)}{2}\frac{\gamma_i}{\sqrt{\gamma_i^{LW}}} = \sqrt{\gamma_s^{LW}} + \sqrt{\gamma_s^{+}}\sqrt{\frac{\gamma_i^{-}}{\gamma_i^{LW}}} + \sqrt{\gamma_s^{-}}\sqrt{\frac{\gamma_i^{+}}{\gamma_i^{LW}}} \quad (6)$$

Where $\gamma^{LW}$ (LW is total Lifshitz–Van der Walls interaction) refer as non-polar and $\gamma^{AB} = 2\sqrt{\gamma_s^+ \gamma_s^-}$ (AB refers to the acid–base interaction) polar components of surface free energy. In addition, acid component and basic component represented by $\gamma^+$ and $\gamma^-$ respectively, index i refers to different liquids and s refers to solid surface.

In Figure 9, the total surface free energy of coating calculated based on three different combinations of liquids, including one dispersive (diiodomethane) and two polar liquids(deionised water, glycerin, ethylene glycol and formamide). Their results compare with result of acid-base multiple regression method. The combination of one dispersive(non- polar) liquid and two polar liquids produces reasonable value, hence combination of purely dispersive liquid like WGE and WGF are removed from calculation due to their unreasonable large values. The intersection of horizontal line on y axis gives required of surface free energy with standard deviation interval (68.3 %) obtained by acid–base multiple regression method. The surface free energy components are gathered in table 3. The surface free energy $\gamma^{total}$=0.33±0.04 mJm$^{-2}$ was successfully calculated according to the standard three–liquid acid–base and with acid-base multiple regression method.

## 4. Conclusions

In summary, a hierarchical superhydrophobic $CeO_2$ (111) surface was successfully fabricated on Ni20Cr superalloy via a cathodic electrodeposition in galvanic mode and subsequently long-term very high vacuum dehydration treatment. The results indicated that, the optimal condition for fabricating superhydrophobic $CeO_2$ coating, ceria electrodeposited at J=-0.5 mAcm$^{-2}$ on mechanically polished Ni20Cr substrate by 800 paper grit with roughness 0.111µm plus electropolished for 1 minute. The superhydrophobic surface showed a high contact angle CA=151.0±1.2° with Gecko state and a surface free energy $\gamma^{total}$=0.33±0.04 mJm$^{-2}$ as calculated based on acid base regression method. Furthermore, the growth mechanism of dual scale $CeO_2$ texture and the interface model of roughness mechanism were proposed in detail. It is believed that this facile, low-cost, and large-area application method can offer an effective strategy to design inorganic superhydrophobic surface and promising antioxidant and anticorrosion applications on other metallic materials.

## Acknowledgments

The author acknowledges the European Commission for providing the Post Doctorate Fellowship of Dr. Satish Mahadik under the Erasmus Mundus "MOVER" program (Contract number 2011-2595/001-001-EMA2).

## Notes and References

1 S. A. Mahadik, N. D.Hegade, S. C. Gupta, P. B. Wagh. *J. Colloid* Interface Sci. 2013, 405, 262–268.

2 I. Banerjee, R.C. Pangule, R.S. Kane, Adv. Mater. 2011, 23, 690–718.

3 S.A. Mahadik, R.S. Vhatkar, P.B. Wagh, Appl. Surf. Sci. 2013, 277, 67–72.

4 A. Lafuma, D. Quere, Nature. Mater. 2003, 2, 457–460.

5 H.J. Ensikat P. Ditsche-Kuru, C. Neinhuis, W. Barthlott, J. Beilstein, Nanotechnol. 2011, 2, 152–161.

6 S.A. Mahadik, M.S. Kavale, S.K. Mukherjee, A.V. Rao, Appl.Surf. Sci. 2010, 257, 333–339.

7 L. Feng, Y. Song, J. Zhai, B. Liu, J. Xu, L. Jiang, D. Zhu, Angew. Chem. Int. 2003, 42, 800-802.

8 I. Woodward, V. Roucoules, J. P. S. Badyal, Langmuir 2003, 19, 3432-3438.

9 W. Lee, M. Jin, W. Yoo, J. Lee, Langmuir 2004, 20, 7665–7669.

10 Q. Xie, G. Fan, N. Zhao, X. Guo, J. Xu, J. Dong, L. Zhang, Y. Zhang, C.C. Han, Adv. Mater. 2004, 16, 1830–1833.

11 T. Ishizaki,Y. Masuda, M. Sakamoto, Langmuir 2011, 27, 4780–4788.

12 W. Duan, A. Xie, Y. Shen, F.Wang, Ind. Eng. Chem. Res. 2011, 50, 4441–4445.

13 L. Martinez, E. Roman, J.L. de Segovia, S. Poupard, J. Creus, F. Pedraza, Appl. Surf. Sci. 2011, 257, 6202-6207.

14 G. Azimi,, R. Dhiman, H. Kwon, A. T. Paxton, K. K. Varanasi. Nature Mater. 2013, 12, 315-320.

15 Y. Hamlaoui, L. Tifouti, C. Remazeilles, F. Pedraza, Materials Chemistry and Physics 2010,120 172–180.

16 P. Parayanthal, F.H. Pollak, Phys. Rev. Lett. 1984, 52, 1822-1825.

17 U. Holzwarth, N.Gibson, Nat. Nanotechnol. 2011, 6, 534-534.

18 P. Wang, Ind. Eng. Chem. Res. 2011, 50, 1605–1609.

19 B. Bouchaud, J. Balmain, G. Bonnet, F. Pedraza, J. Rare Earth 2012, 20,559-562.

20 B. Bouchaud, J. Balmain, G. Bonnet, F. Pedraza, Electrochim. Acta 2013, 88, 798–806.

21 M.A. Arenas, J.J. de Damborenea, Electrochim. Acta 2003, 48, 3693-3698.

22 Q. Yuan, Y-W. Zhang, C-H. Yan, J.Colloid. Interf. Sci. 2009, 335, 151–167.

23 L. Arurault, P. Monsang, J. Salley, R.S. Bes, Thin Solid Films 2004, 446, 75–80.

24 I. Zhitomirsky, A. Petric, Ceram. Int. 2001, 27, 149–155.

25 O. Lebedeva, G. Dzhungurova, A. Zakharov, D. Kultin, L. Kustov, V. Krasovskii, K. Kalmykov, S. Dunaev, ACS. Appl. Mater. Interfaces 2013, 5, 10551−10558.

26 S. Khan, G. Azimi, B. Yildiz, K. K. Varanasi, Appl. Phys. Lett. 2015, 106:061601, 1-5.

27 R. David, P. M. Mullins, C. Tsung-Liang, C.C. Florencia, D. B. Michael, M. C. Hans, H. O. Steven, J. Phys. Chem. C. 2012, 116, 19419−19428.

28 R. N. Wenzel, Ind. Eng. Chem. 1936, 28, 988-994.

29 A. B. D. Cassie, S.Baxter, Trans. Faraday Soc. 1944, 40, 546 – 561.

30 X. Chen, J. A. Weibel, S. V. Garimella, Adv. Mater. Interf. DOI:10.1002/((admi.201400480)).

31 K.J. Kubiak, M.C.T. Wilson, T.G. Mathia, P. Carval, Wear 2011, 271, 523–528.

32 L. Xu, R. G. Karunakaran, J. Guo, S. Yang, ACS. Appl. Mater. Interfaces 2012, 4, 1118−1125.

33 Y. Hamlaoui, F. Pedraza, C. Remazeilles, S. Cohendoz, C. Rébéré, L. Tifouti, J. Creus, Mater. Chem. Phys. 2009, 113, 650–657.

34 J. Adams,V. Schilfgaarde, J. Chem. Phys. 2005,123, 064701-064710.

35 M. Fronzi, S. Piccinin, B. Delley, Phys. Chem. 2009, 11, 9188–9199.

36 V.F. Solovyov, T. Ozaki, A. Atrei, L. Wu, A. Al-Mahboob, J.T. Sadowski, X. Tong, D. Nykypanchuk, Q. Li Sci. Rep. 2014, 4:4627, 1-8.

37 M.A. Borowiak, M.H. Jamroz, R. Larsson, J. Mol.Catal. A: Chem. 1999, 139, 97−104.

38 F. Zhang, P. Wang, J. Koberstein, S. Khalid, S. Chan, Surf. Sci. 2004, 563, 74–82

39 F. Harbach,F. Fischer, J. Phys. Chem. Solids 1975, 36, 601–603.

40 Z. Navratil, V. Bursikova, P. Stahel, M. Sira, P. Zverina, Czech. J. Phys. 2004, 54, 877-882.

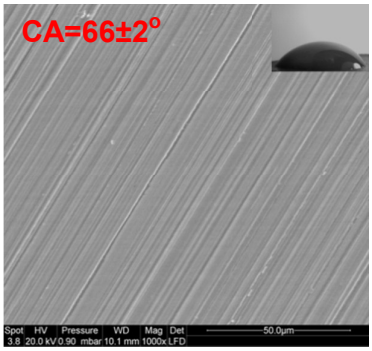


(a) mechanical polishing

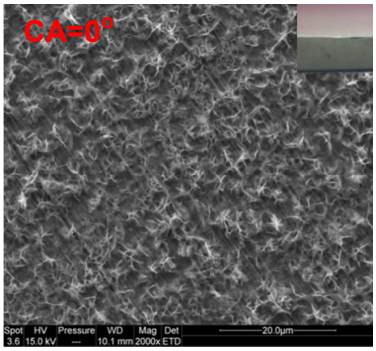


(b) deposit on electropolished surface

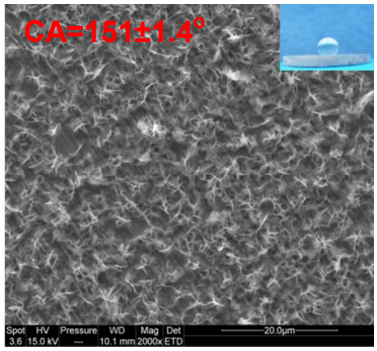


(c) deposit on electropolished surface after vacuum relaxation

**Graphical Abstract**

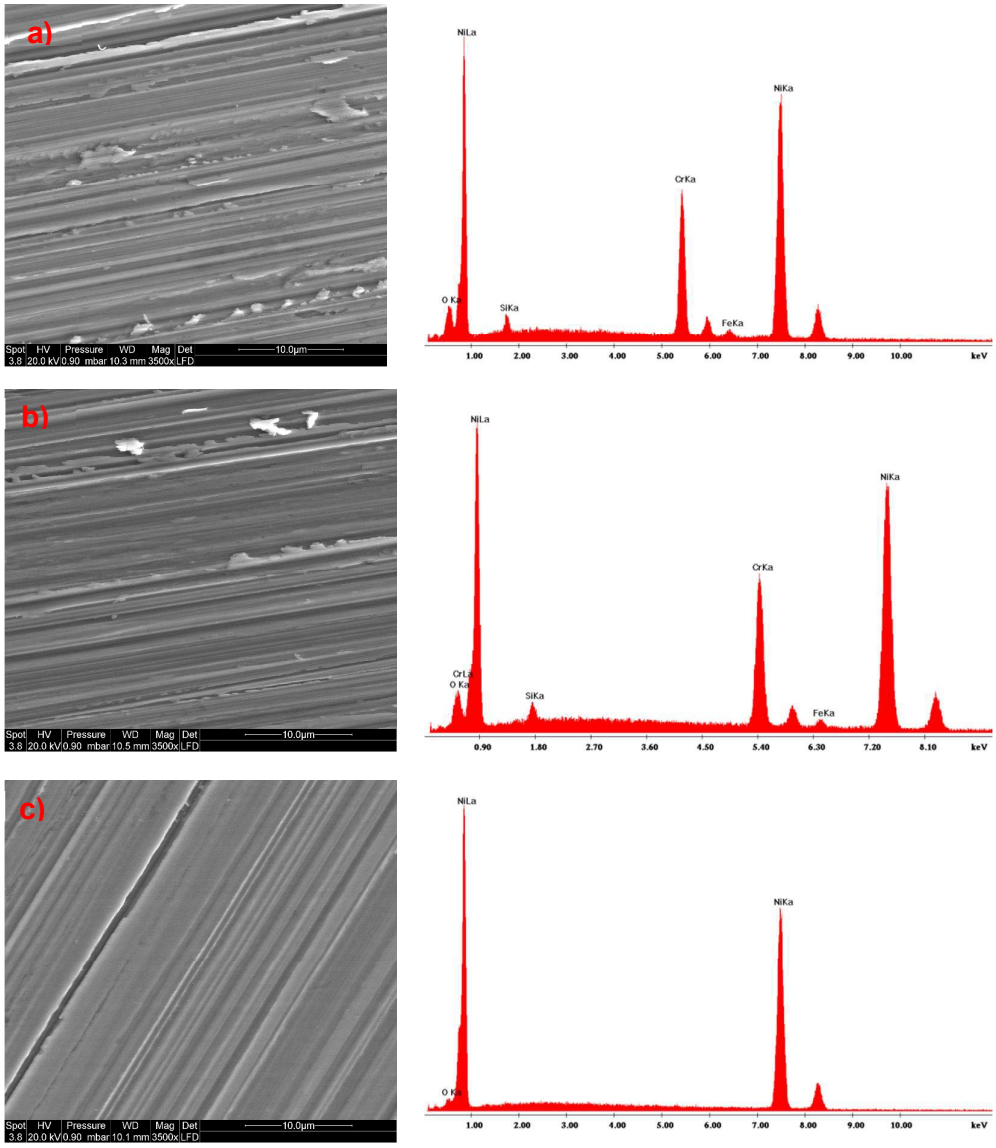


**Figure 1.** Effect of electropolishing period on surface morphology and surface composition at a) 1 min b) 2 min c) 5 min.

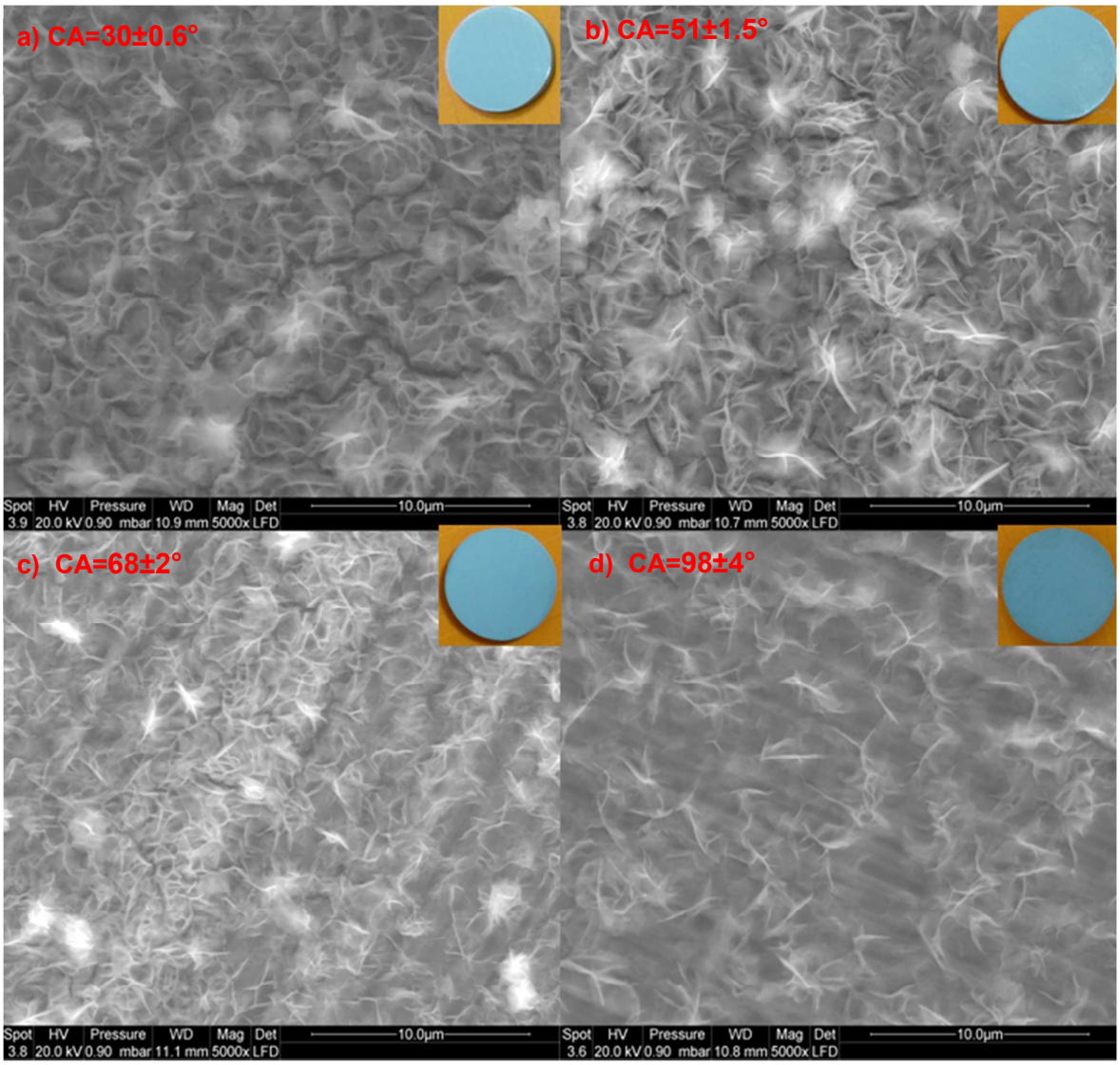


**Figure 2.** Evolution of surface morphology of the cerium oxide coatings deposited at J=-0.5 mAcm$^{-2}$, 10 min and different electropolishing period a) without electropolishing (0 min) b) 1 min c) 2 min d) 5 min.

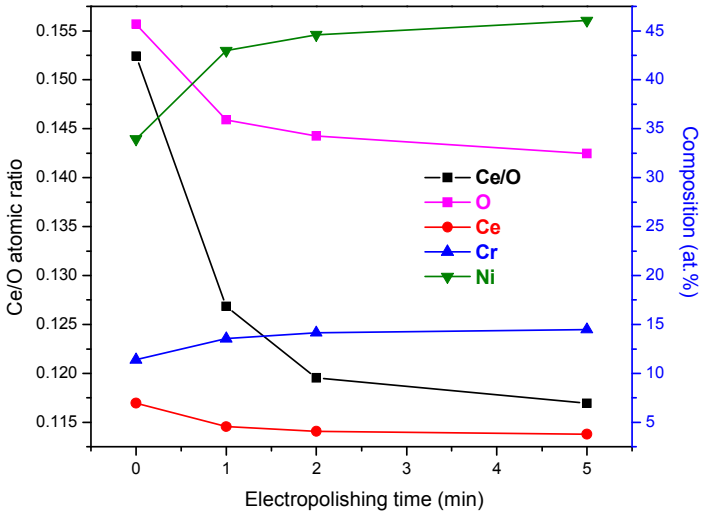


**Figure 3.** Effect of electropolishing period of an electrodeposited ceria surface on the Ce/O. NB: the zero point corresponds to the as-mechanically polished, i.e. without electropolishing.

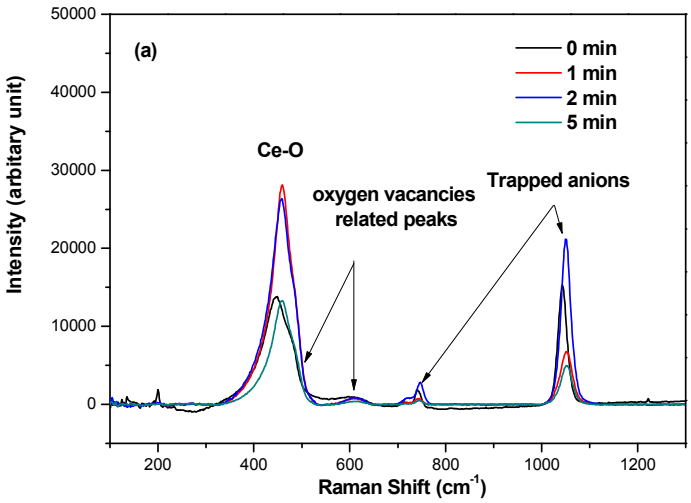

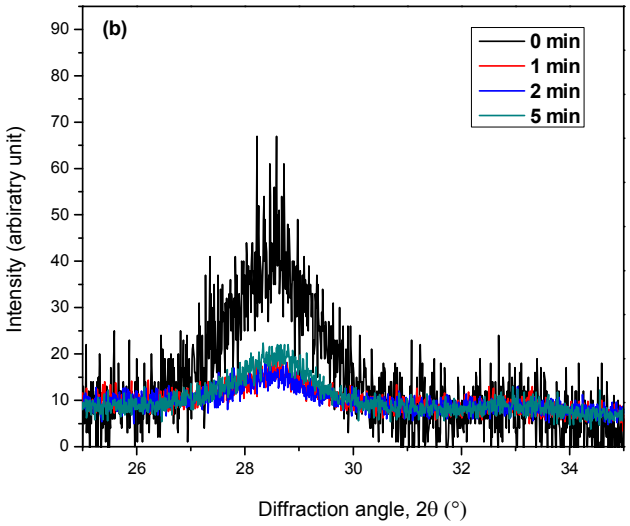


**Figure 4.** Effect of electropolishing period of the cerium oxide coating electrodeposited at J= -0.5 mAcm$^{-2}$, 10 min. (a) Variation of surface defect with electropolishing period calculated according to Raman analysis. (b) Variation of crystal size with electropolishing period calculated using XRD pattern.

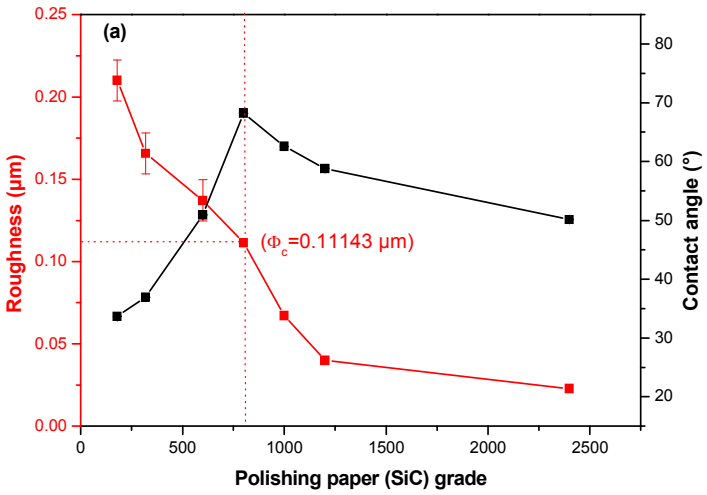

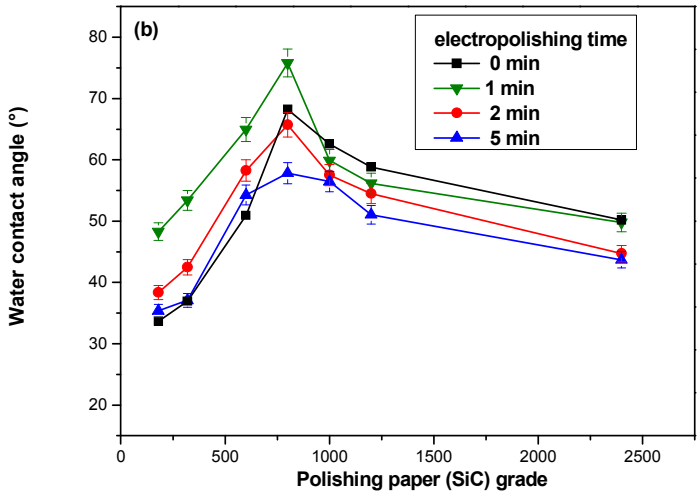


**Figure 5.** Water contact angles (interface model) as a function of surface preparation (a) correlation between roughness and SiC paper grade (mechanical polishing) and (b) correlation between electropolishing and paper grade (mechanical polishing).

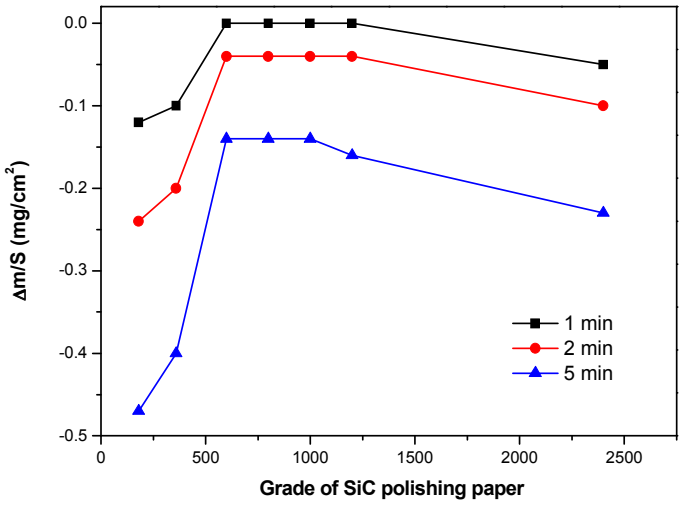


**Figure 6.** Influence of electropolishing periods on mass variation.

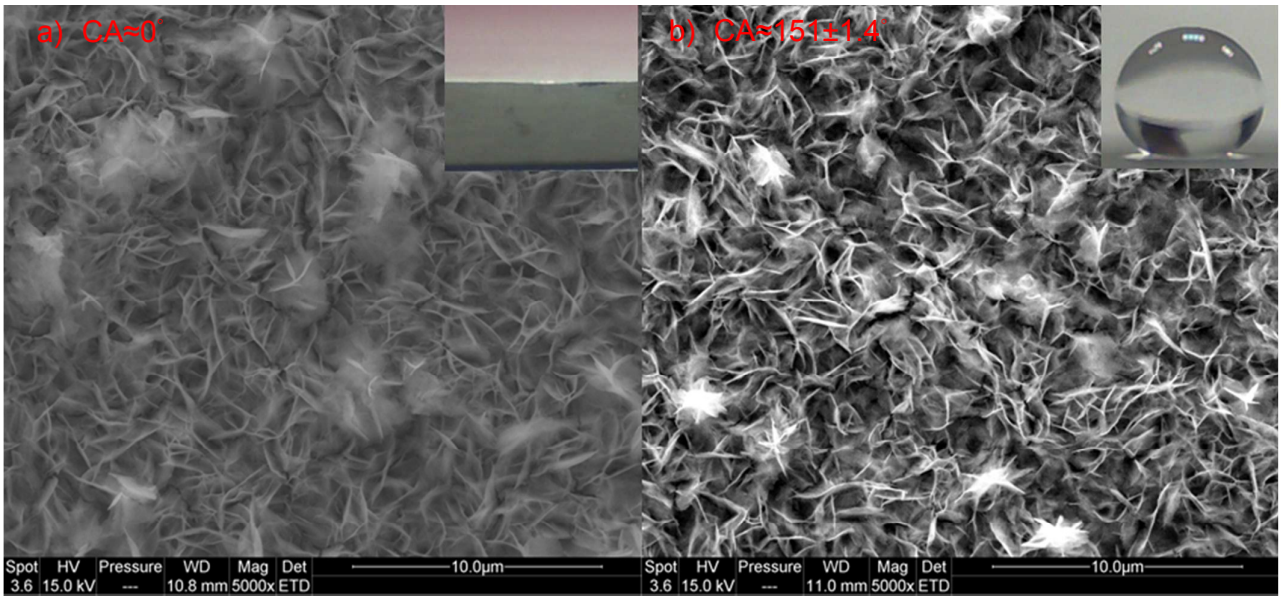


**Figure 7.** SEM morphology for the cerium oxide films deposited at J=-0.5 mAcm$^{-2}$, 10 min plus 1 minute electropolishing on mechanical polished substrate (SiC# 800). a) Before UVH surface relaxation. b) After UVH surface relaxation.

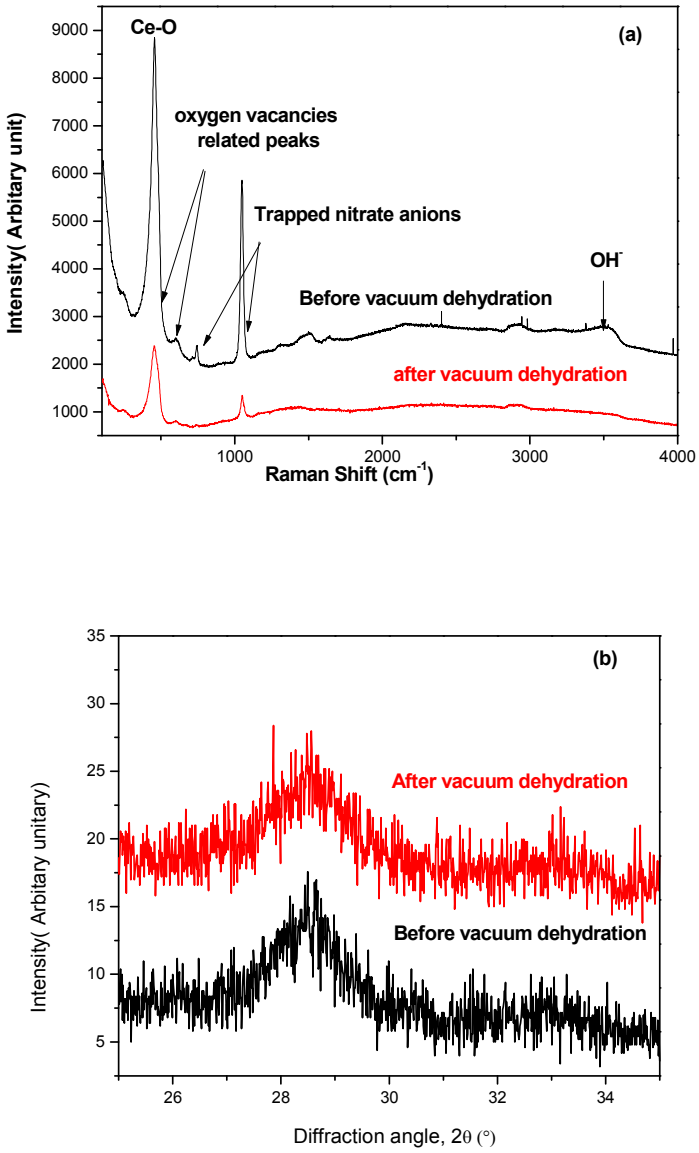


**Figure 8.** Characterization of cerium oxide coating electrodeposited at J= -0.5 mAcm$^{-2}$, 10 min, plus 1 min electropolishing on mechanical polished substrate (SiC# 800) before and after vacuum relaxation. (a) Raman analysis. (b) X-ray patterns.

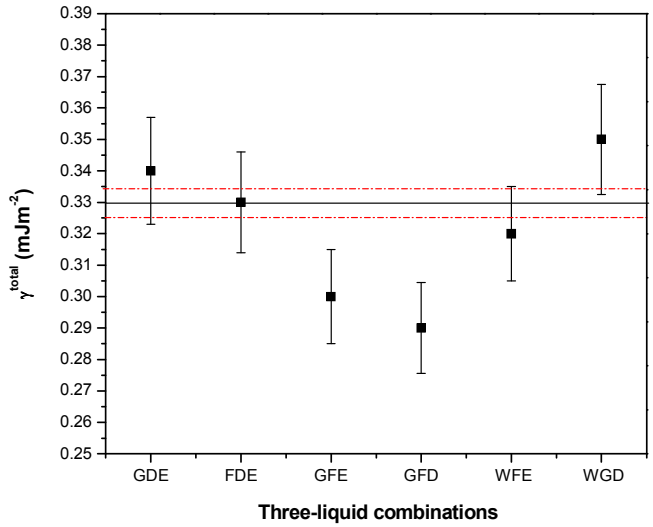


**Figure 9.** The total coating surface energy retrieved based on standard three–liquid acid–base method. The horizontal dotted red line represents the value and standard deviation interval (68.3 %) obtained by acid–base multiple regression method. The letters denote liquids in following way: W – water, G – glycerol, E – ethylene glycol, D – diiodomethane, F – formamide, triads.

## List of Tables

**Table 1.** The effect of electropolishing period on crystal size of electrodeposited ceria coating based on XRD and Raman analysis.

| Electropolishing periods (min) | Crystallite size (nm) | | Vacancies density ($10^{22}$ $cm^{-3}$) (±0.027) |
|---|---|---|---|
| | XRD (±0.10) | Raman (±0.06) | |
| 0 | 4.20 | 3.42 | 2.13 |
| 1 | 4.41 | 4.50 | 1.61 |
| 2 | 4.53 | 4.67 | 1.55 |
| 5 | 4.88 | 4.91 | 1.47 |

**Table 2.** The effect of long–term UVH surface relaxation on surface defects for electrodeposited ceria coating on an optimal conditions of surface preparation (SiC#800 + electropolishing for 1 min).

| Optimal conditions | Crystallite size (nm) | | Vacancies density ($10^{22}$ $cm^{-3}$) (±0.027) |
|---|---|---|---|
| | XRD (±0.10) | Raman (±0.06) | |
| Before vacuum dehydration | 4.12 | 3.87 | 1.88 |
| After vacuum dehydration | 4.79 | 4.69 | 1.54 |

**Table 3.** Surface energy values calculated by acid-base multiple regression method with 5 liquids. Error values were determined by fitting for a confidence level of 68.3 %.

| Liquids | Angle (◦) | Acid-base multiple regression method | | | | |
|---|---|---|---|---|---|---|
| | | $\gamma^{Total}$ ($mJ/m^2$) | $\gamma^{LW}$ ($mJ/m^2$) | $\gamma^{AB}$ ($mJ/m^2$) | γ− ($mJ/m^2$) | γ+ ($mJ/m^2$) |
| Water | 151.0 ± 1.4 | 0.33 ± 0.04 | 0.29 ± 0.03 | 0.04± 0.02 | 0.00± 0.00 | 0.12 ± 0.03 |
| Glycerol | 149.5 ± 1.1 | | | | | |
| Formamide | 149.0 ± 1.3 | | | | | |
| Diiodomethane | 147.9 ± 0.5 | | | | | |
| Ethylene glycol | 147.3 ± 0.7 | | | | | |